

Three-dimensional fluorescence lifetime tomography

Anuradha Godavarty^{a)}

327 Votey Building, Department of Computer Science, University of Vermont, Burlington, Vermont 05405

Eva M. Sevick-Muraca

1011 Richardson Building, Photon Migration Laboratories, Texas A&M University, College Station, Texas 77843

Margaret J. Eppstein

327 Votey Building, Department of Computer Science, University of Vermont, Burlington, Vermont 05405

(Received 20 August 2004; revised 19 December 2004; accepted for publication 23 December 2004; published 18 March 2005)

Near-infrared fluorescence tomography using molecularly targeted lifetime-sensitive, fluorescent contrast agents have applications for early-stage cancer diagnostics. Yet, although the measurement of fluorescent lifetime imaging microscopy (FLIM) is extensively used in microscopy and spectroscopy applications, demonstration of fluorescence lifetime tomography for medical imaging is limited to two-dimensional studies. Herein, the feasibility of three-dimensional fluorescence-lifetime tomography on clinically relevant phantom volumes is established, using (i) a gain-modulated intensified charge coupled device (CCD) and modulated laser diode imaging system, (ii) two fluorescent contrast agents, e.g., Indocyanine green and 3-3'-Diethylthiatricarbocyanine iodide differing in their fluorescence lifetime by 0.62 ns, and (iii) a two stage approximate extended Kalman filter reconstruction algorithm. Fluorescence measurements of phase and amplitude were acquired on the phantom surface under different target to background fluorescence absorption (70:1, 100:1) and fluorescence lifetime (1:1, 2.1:1) contrasts at target depths of 1.4–2 cm. The Bayesian tomography algorithm was employed to obtain three-dimensional images of lifetime and absorption owing to the fluorophores. © 2005 American Association of Physicists in Medicine.
[DOI: 10.1118/1.1861160]

I. INTRODUCTION

Optical-based molecular imaging and tomography using near-infrared (NIR) fluorescent contrast agents represents an emerging technology, which may advance cancer diagnostic imaging. In optical imaging, NIR light between 700–900 nm wavelengths propagates deeply into tissues and can differentiate diseased from normal tissues based on the differences in the endogenous absorption owing to oxy- and deoxy-hemoglobin, as demonstrated from breast imaging studies.^{1–7} In order to increase the optical detection of small tissue lesions not contrasted by neovascularization, molecular targeting and reporting fluorescent contrast agents have been developed. These agents can potentially improve the target:background (T:B) optical contrast ratio between normal and diseased tissues with greater specificity and sensitivity over optical imaging performed using endogenous absorption contrast alone.^{8–10}

In recent years, three-dimensional (3D) fluorescence-enhanced optical tomography has been developed for time-dependent and time-independent measurements of light propagation for *in vivo* small animal studies^{11,12} and large phantom studies.^{13–19} All developments have been based upon T:B contrast due to fluorophore absorption cross section. Yet fluorescence offers the added capability of determining lifetime or radiative decay kinetics as a method for assessing the local environmental conditions independent of fluorophore concentration.^{20,21} Hence, by employing lifetime-sensitive fluorescing contrast agents, tomographic

analysis of the fluorescence measurements may differentiate diseased tissues from normal tissues. Pioneering work to develop “reporting” fluorophore-protein conjugate contrast agents that demonstrate changes in fluorescence decay kinetics in the presence of specific proteases has been reported by Weissleder and colleagues^{22–24} and is the subject of development in other laboratories.²⁵

Tomographic imaging of fluorescence lifetime in 2D^{26–28} and 3D^{29,30} has been demonstrated from time-dependent simulated measurements. While 3D tomographic reconstruction of lifetime-sensitive fluorophore absorption cross section has been experimentally reported from time-independent measurements on small animals,³¹ fluorescence lifetime tomography has been limited to 2D experimental studies using time-dependent measurement schemes.³² To date, 3D fluorescence lifetime tomography has not been demonstrated using experimental measurements, but has been limited to simulated studies.^{29,30}

In this contribution, the feasibility of 3D fluorescence lifetime tomography is demonstrated on clinically relevant tissue phantoms using fluorescent contrast agents differing in their fluorescence optical properties and time-dependent (frequency-domain) fluorescence measurements. Clinical translation of 3D fluorescence lifetime tomography will require both: (i) the development of lifetime sensitive fluorescent contrast agents, which “report” environmental conditions through a change in decay kinetics and (ii) the development and demonstration of a tomography algorithm that can reconstruct the 3D distribution of spatially-varying

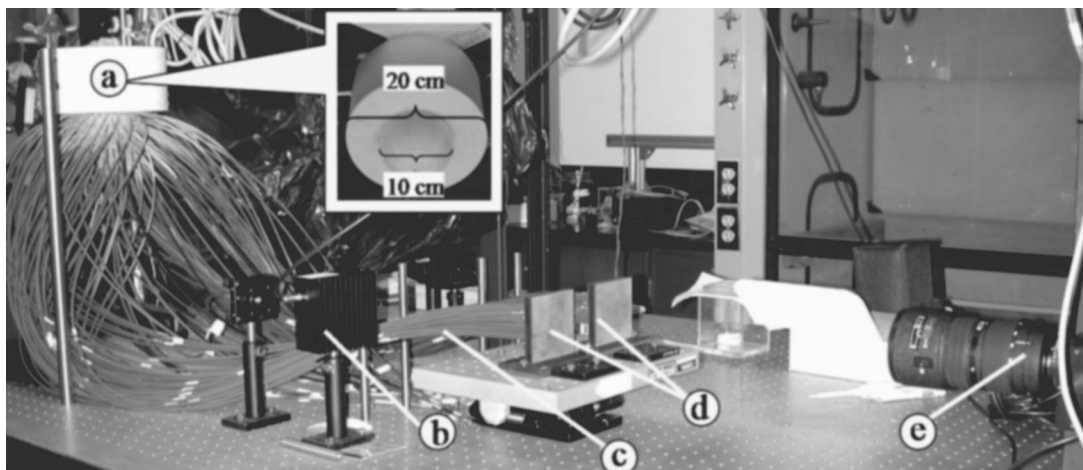


FIG. 1. Schematic of the gain-modulated intensified CCD imaging system using a breast-shaped tissue phantom. Frequency-domain experiments are performed using 100 MHz modulated light source, launched *via* optical fibers. The different components in the schematic include: (a) breast-shaped tissue phantom; (b) laser diode (source); (c) collecting optical fibers; (d) interfacing plates; and (e) intensified CCD camera lens.

fluorescence lifetime from experimental measurements (using clinically relevant volumes). While the former is a subject of active research in a variety of laboratories,^{22–24} the focus of the current work is the latter. Herein, we use two dyes whose decay properties (in terms of fluorescence lifetime and quantum efficiency) are known and constant in order to assess the success of the reconstruction algorithm in identifying regions of varying fluorescence lifetime.

Experiments were performed under various conditions of T:B optical contrast ratios in fluorescence absorption (concentration) and lifetime using two contrast agents (Indocyanine Green, ICG, and 3-3' Diethylthiatricarbocyanine Iodide, DTTCI) similar in their excitation and emission spectra (780 and 830 nm, respectively), but different in their fluorescence lifetime. A 3D image reconstruction algorithm was developed using a two-stage Bayesian approximate extended Kalman filter (AEKF). Reconstruction of both fluorescence lifetime and absorption cross-section contrast was investigated, and the results demonstrate the feasibility of 3D fluorescence lifetime tomography.

II. MATERIALS AND METHODS

A. Breast-mimicking phantoms

Experimental studies were carried out using a hollow breast-shaped phantoms (10 cm diameter hemispherical phantom “breast” atop a 20 cm cylindrical base phantom

“chest wall” as shown in Fig. 1) filled with 1087 cm³ of a fatty emulsion solution (1% Liposyn, Abbott Laboratories, North Chicago, IL), with optical properties (experimentally acquired³³) similar to those of the normal human breast tissue.

In order to demonstrate the potential benefit of future lifetime-sensitive dyes currently under development, two well-characterized NIR dyes of known and constant lifetime (that mimic the fluorescence decay kinetic change between a target and its surroundings) were chosen for our tomographic imaging studies under well-controlled conditions in a clinically relevant breast phantom. The fluorophores used were (i) ICG stabilized with sodium polyaspartate (MW 3000–8000) (Sigma-Aldrich Chemical Co., St. Louis, CO)³⁴ and diluted in deionized water and 1% Liposyn solution, and (ii) DTTCI diluted in dimethyl sulfoxide and 1% Liposyn solution. The dyes were used in appropriately contrasting micromolar concentrations in the background of the phantom and inside a 1 cm³ clear acrylic target suspended inside the hemispherical portion of the phantom. ICG and DTTCI were chosen primarily because their fluorescent decays are well described by single-exponential decay functions,²⁰ and the two contrast agents have a roughly twofold difference in fluorescence lifetime, τ ($\tau_{\text{ICG}}=0.56$ ns, $\tau_{\text{DTTCI}}=1.18$ ns).³⁴ Since ICG and DTTCI excite and emit at similar wavelengths, but have different fluorescence lifetime (τ), they were used in different T:B fluorescence absorption (70:1, 100:1) and life-

TABLE I. Experimental case studies performed using a single 1 cc target located at various depths, under varying T:B contrasts in fluorescence absorption ($\mu_{a_{x \rightarrow m}}$) and lifetime (τ).

Case	T depth (cm)	T:B dye	T:B Absorption	T:B Lifetime
1	1.4	ICG : ICG	100 : 1	1 : 1
2	2.0	ICG : ICG	100 : 1	1 : 1
3	1.4	DTTCI : ICG	70 : 1	2.1 : 1

TABLE II. Background optical absorption (μ_a) and reduced scattering (μ'_s) coefficients of 1% Liposyn solution in tissue phantoms at excitation (subscript x) and emission (subscript m) wavelengths due to fluorophore (subscript f) and nonfluorescing chromophore (subscript i), for the different experimental cases studied. All the units are in cm⁻¹.

Case	μ_{axi}	μ_{ami}	$\mu_{a_{x \rightarrow m}}$	μ_{ami}	μ'_{sx}	μ'_{sm}
1&2	0.025	0.032	0.003	5e-4	10.88	9.82
3	0.023	0.030	0.003	5e-4	9.99	9.67

time contrast ratios (1:1, 2.1:1), and target depths (1.4–2 cm) in order to perform experimental studies under three different cases as shown in Table I. The background optical properties of the 1% Liposyn solution in the phantom are provided for each experimental case in Table II. ICG and DTTCl also have differing quantum efficiency, ϕ ($\phi_{\text{ICG}}=0.016$, $\phi_{\text{DTTCl}}=0.034$). However, the quantum efficiency of the dye placed in the acrylic target was reduced by 32% due to the transmission efficiency of the acrylic container, leading to a small T:B ϕ contrast in the current studies (0.68:1 for Cases 1 and 2, and 1.44:1 for Case 3). Hence, the T:B contrast in quantum efficiency was neglected in the current studies and is further described in Sec. II C.

B. Instrumentation

Time-dependent measurement techniques (i.e., time- or frequency-domain) are required for lifetime imaging, since the fluorescence lifetime information is preserved as delayed pulse time in the time-domain method, or as phase shift measurements in frequency-domain method (as employed in our current studies).

Herein, frequency-domain photon migration (FDPM) fluorescence measurements were obtained from the hemispherical surface of the clinically relevant phantom. Initially, modulated excitation light at 100 MHz was used to sequentially illuminate the phantom surface (783 nm) via 27 multimode optical fibers (1 mm diameter, model FT-1.0-EMT, Thorlabs Inc., NJ). The modulated excitation light propagated in the phantom medium and upon encountering the fluorescent molecules, generated modulated fluorescence signals (100 MHz, 830 nm), which further propagated in the phantom medium before they were simultaneously collected from various locations on the phantom surface via 128 multimode optical fibers. The free ends of the optical fibers collecting the fluorescence light on the phantom surface were mounted as 2D arrays on two interfacing plates (64 collection fibers each), which were imaged using a gain-modulated intensified charge coupled device (ICCD) camera (i.e., optically coupled image intensifier and CCD camera). An optical filter assembly containing appropriate filters (830-nm interference filter and holographic notch filter) was used to minimize the excitation light leakage, rejecting light outside the bandwidth of the emission wavelength; thus allowing predominantly the fluorescence light to be imaged by the photocathode of the image intensifier. The photocathode of the image intensifier (FS9910C, ITT Night Vision, VA) was modulated at the same frequency (100 MHz) as the incident NIR excitation light. The acquired modulated fluorescence signal was collected as steady-state intensity signal by the integrating CCD camera (CCD-512-EFT Photometric CH12, Roper Scientific, Trenton, NJ) via homodyne mixing techniques and low pass filtering caused by the slow phosphor output of the image intensifier. The phosphor output was sensitive to the phase delay existing between the two phase-locked oscillators (Marconi Instruments model 2022D, UK; and Programmed Test Sources model 310M201GYX-53, Littleton, MA) that modulated the incident NIR excitation

light and the photocathode of the image intensifier, respectively. By varying the phase delay between the two oscillators from 0 to 2π , the steady-state intensities at each pixel of the CCD image varied sinusoidally. Upon performing fast Fourier transforms to the acquired CCD images, measurements of amplitude (I_{ac}) and phase shift (θ) of the fluorescence signal at each collection fiber location were acquired. Five sets of images of the interfacing plates were acquired and averaged in order to assess as well as reduce the measurement error of the imaging system. The fluorescence measurements acquired from each interfacing plate (i.e., 64 collection fibers) and for a given point source illumination, were referenced (by dividing each measurement with respect to the measurement containing the maximum fluorescence I_{ac}) in order to account for the instrument effects.^{14,16–18} These referenced fluorescence measurements were thus used in terms of (i) the logarithm of the referenced amplitude, denoted by $\ln(\text{ACR})$ and (ii) the referenced phase shift, denoted by RPS, during image reconstructions. Only measurements above the noise floor [modulation depth (ac/dc) ≥ 0.025] were employed during image reconstructions. A schematic of the instrumentation is shown in Fig. 1. Further details about the instrument setup and the data acquisition procedures are provided elsewhere.¹⁶

C. Image reconstruction algorithm

FDPM fluorescence measurements were collected in response to sequential NIR point source illuminations and inverted to tomographically estimate 3D spatial distributions of the fluorescence optical properties using the coupled diffusion equations^{35–37} (see Appendix A for details) and a computationally efficient variant of the approximate extended Kalman filter (AEKF) algorithm, as described below.

A dynamic recursive estimate of the unknown parameters (i.e., fluorescence optical properties) and the parameter error variances were evaluated using (i) experimental referenced measurements regularized by empirically determined measurement error variance (i.e., variance of the repeated measurements), (ii) a static estimate of model error variance (estimated to be 1/4 of the mean of measurement error variance), and (iii) a forward simulator that computes predicted referenced measurements by employing a diffusion approximation of the coupled radiative transport equations for excitation and emission light.^{35–37} The forward simulator (see Appendix A for details) was implemented using a fast vectorized finite element technique³⁸ containing 6956 nodes, of which only parameters associated with the $n=3857$ nodes in the hemispherical portion of the model were allowed to vary (i.e., the number of unknowns during reconstruction of each optical parameter was 3857). Given the estimates of the measurement error, model error, and initial parameter estimation errors, the AEKF algorithm minimizes the parameter error variance, as opposed to simply minimizing the parameter error, thereby regularizing this ill-posed problem in a Bayesian manner. Details of the AEKF algorithm used in the current study are provided as supplemental information (Appendix B) and are further elaborated elsewhere.^{14,16,28}

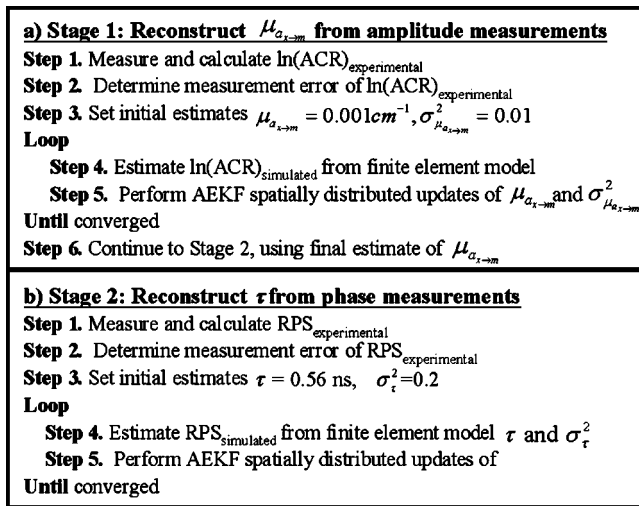


FIG. 2. Flowsheet of the two-stage image reconstruction algorithm.

The source of fluorescence emissions is governed by the spatial distribution of fluorescence absorption cross-section ($\mu_{a_{x \rightarrow m}}$), fluorescence lifetime (τ), and quantum efficiency (ϕ) (as shown in Eq. (A2) of Appendix A). Spatial variance in $\phi \mu_{a_{x \rightarrow m}}$ (i.e., the amount of absorption and quantum efficiency of the dye) predominantly influences the fluorescence amplitude measurements (in frequency-domain imaging system), since $\mu_{a_{x \rightarrow m}}$ and ϕ determine the intensity of the emitted fluorescence in the presence of an excitation light source. On the other hand, spatial variance in the fluorescence lifetime predominantly impacts the phase-delay (θ) of the fluorescent source, i.e., $\theta \sim \tan^{-1}(\omega\tau)$, in a frequency-domain system with ω frequency.³⁹ Hence fluorescence amplitude measurements were used to estimate the spatial distribution of $\mu_{a_{x \rightarrow m}}$ [assuming a homogeneous and constant quantum efficiency (ϕ) distribution] and fluorescence phase delay measurements were used to estimate the spatial distribution of τ . The quantum efficiency distribution was assumed homogeneous and constant because an under-(over-) estimate of fluorescence absorption cross-section compensates for an over-(under-) estimate of quantum efficiency in the emission source term, as both these parameters impact the same measured quantity (i.e., fluorescence amplitude). However, the T:B contrast in ϕ was relatively small [0.68:1 for Cases 1 and 2, and 1.44:1 for Case 3 (see Sec. II A)] in comparison to the T:B contrast in $\mu_{a_{x \rightarrow m}}$ (100:1 for Cases 1 and 2, and 70:1 for Case 3), and hence the assumption of a homogeneous and constant ϕ -distribution was considered.

Simultaneous reconstruction of both $\mu_{a_{x \rightarrow m}}$ and τ was not carried out since: (i) *a priori* knowledge of the fluorescence absorption ($\mu_{a_{x \rightarrow m}}$) distribution is significant for estimation of the fluorescence lifetime distribution, especially when the fluorescence concentration (or absorption) contrast increases and (ii) the intense computations prohibited the simultaneous coestimation of two unknown parameters in large phantom volumes. Thus, a two-stage image reconstruction approach (see Fig. 2) was developed in order to reconstruct $\mu_{a_{x \rightarrow m}}$ in stage-1 and τ in stage-2.

In stage-1 reconstructions [Fig. 2(a)], amplitude measurements, $\ln(\text{ACR})$ are used to reconstruct the absorption cross section of the fluorophore by (i) first assuming a low initial estimate in $\mu_{a_{x \rightarrow m}} = 0.001 \text{ cm}^{-1}$ that was different from the true experimental background ($\mu_{a_{x \rightarrow m}} = 0.003 \text{ cm}^{-1}$) and (ii) assuming a constant fluorescence lifetime ($\tau = 0.56 \text{ ns}$) and constant quantum efficiency ($\phi = 0.016$), which are equivalent to the fluorescence properties of the background fluorophores. During stage-1 reconstructions, the AEKF algorithm employed measurements of $\ln(\text{ACR})$ in order to estimate the fluorescence absorption cross-section $\mu_{a_{x \rightarrow m}}$, which was constrained by means of pseudo-beta transforms²⁸ to the range of $0.0 < \mu_{a_{x \rightarrow m}} < 0.8 \text{ cm}^{-1}$ during inversions. The fluorescence absorption coefficient at the emission wavelength μ_{amf} was assumed equal to $0.1692 \times \mu_{a_{x \rightarrow m}}$ for the entire phantom, based on the ratio of the extinction coefficients of the background fluorophores (i.e., ICG in all the experimental cases) at excitation ($\epsilon_{780 \text{ nm}} = 130\,000 \text{ M}^{-1} \text{ cm}^{-1}$) and emission wavelengths $\epsilon_{830 \text{ nm}} = 22\,000 \text{ M}^{-1} \text{ cm}^{-1}$.²⁹ Reconstructions were carried out using a uniform initial parameter variance estimate ($\sigma_{\mu_{a_{x \rightarrow m}}}^2 = 0.01$) for the transformed $\mu_{a_{x \rightarrow m}}$. Stage-1 reconstructions were assumed to have converged when there was less than a 1% decrease in the root mean square $\ln(\text{ACR})$ error between consecutive iterations. The spatial distribution of the absorption cross section of the fluorophore $\mu_{a_{x \rightarrow m}}$ determined in stage-1 was then used as an input into stage-2 reconstructions.

In stage-2 reconstructions [Fig. 2(b)], phase shift (RPS) measurements were used to reconstruction the fluorescence lifetime by (i) first assuming an initial guess of the fluorescence lifetime (τ) equivalent to that of the background fluorophore ($\tau = 0.56 \text{ ns}$), (ii) considering the spatial distribution of absorption cross-section $\mu_{a_{x \rightarrow m}}$ determined from stage-1, and (iii) assuming a constant quantum efficiency ($\phi = 0.016$) equivalent to the background fluorophore. During stage-2 reconstructions, the AEKF algorithm employed measurements of RPS in order to estimate $\omega\tau$ (i.e., product of fluorescence lifetime and modulation frequency [$\omega = 100 \text{ MHz}$]), which was constrained by means of pseudobeta transforms to the range of $0.48 < \tau < 1.27 \text{ ns}$ during inversions. The multiplication of τ with the constant ω was used to prevent numerical truncation error. Reconstructions were carried out using a uniform initial parameter variance estimate ($\sigma_{\tau}^2 = 0.2$) for the transformed $\omega\tau$. Stage-2 reconstructions were assumed to have converged when there was less than a 0.5% change in the maximum RPS error between consecutive iterations.

Three-dimensional image reconstructions were carried out on a Dell Workstation PWS650 [Xeon(TM) 3.06 GHz, 2.0 GB RAM], and required less than 1 s per iteration per fluorescence measurement (for a single point source illumination), for each stage of the reconstruction. The distribution of the remaining optical parameters, such as (i) absorption coefficient due to nonfluorescing chromophores and (ii) scattering coefficients due to fluorophores and nonfluorescing chro-

TABLE III. Mean and/or variance of model mismatch and measurement errors for the three experimental cases (using measurements above noise floor).

Case	Number of meas above noise	Model mismatch error				Measurement error	
		Mean ln(ACR)	Variance ln(ACR)	Mean RPS	Variance RPS	Variance ln(ACR)	Variance RPS
1	401	0.14	0.36	0.18	0.73	0.0008	0.11
2	480	0.16	0.81	0.23	0.81	0.0006	0.11
3	1068	0.24	0.73	0.06	0.03	0.0005	0.004

morphores [shown in Eq. (A2) of Appendix A], were assumed homogeneous and known (Table II) for each experimental case and for both the reconstruction stages.

D. Model and measurement error calculation

In any inversion technique, the estimation of the model mismatch errors (difference between experimental and simulated measurements) is important in validating the light propagation model used in the forward simulator of the reconstruction algorithm. Herein, model mismatch errors in ln(ACR) and RPS were computed for each fluorescence measurement whose measured modulation depth was above the

noise floor (i.e., $ac/dc \geq 0.025$). The mean of the model mismatch error thus represents (i) model bias and (ii) any residual bias in the measurement error obtained after averaging the measurement repetitions. Measurement error variances were experimentally estimated as the variance of the mean of five repeated measurements of ln(ACR) and RPS obtained for each fluorescence measurement, whose measured modulation depth was above the noise floor.

III. RESULTS AND DISCUSSION

A. Model and measurement errors

Lumped statistics for both model mismatch and measurement errors are given in Table III. By definition, measurement errors were zero mean, with all bias combined into the mean of the model mismatch error. Model and measurement error variances for ln(ACR) are the same order of magnitude for all three cases. However, when a lifetime contrast was introduced in the tissue phantom (Case 3 of Table I), the increase in fluorescence lifetime in the target region resulted in an increase in phase shift at the phantom surface, producing a stronger perturbation in the acquired phase shift signal. Consequently, with lifetime contrast (Case 3), the RPS variances of both model and measurement errors were reduced by an order of magnitude, relative to the no-lifetime contrast experimental cases (Cases 1 and 2 of Table I). In experimental cases 1 and 2, all the collection fibers in the region of the target were attached to one interfacing plate, so measurements were made at 64 collection fibers for each source illumination. In Case 3 collection fibers from both the interfacing plates were close to the target, so measurements were made at 128 collection fibers for each source illumination. Thus, the larger number of measurements and the stronger fluorescence signal strength in Case 3 resulted in a larger usable data set than in Cases 1 and 2, as shown in Table III.

B. Three-dimensional fluorescence absorption tomography

In all the three experimental cases, the 3D reconstructed fluorescence absorption $\mu_{a_{x \rightarrow m}}$ distributions identified the targets close to their true location in the experiments as shown in Fig. 3 as 3D iso-surface plots of the $\mu_{a_{x \rightarrow m}}$ distribution. All these stage-1 reconstructions converged in 12–13 iterations, and the sum of squared ln(ACR) prediction errors dropped between 86% and 92% in each case [see Fig. 4(a)]. Nonetheless, the reconstructed $\mu_{a_{x \rightarrow m}}$:T:B ratios were not quantitatively accurate (Table IV), reflecting the relative insensitivity of this convergence metric to absolute $\mu_{a_{x \rightarrow m}}$ values. These results are consistent with our earlier studies^{14,16–19} showing that locations of contrasting fluorescence absorption can be reconstructed with greater accuracy than the absolute values of fluorescence absorption ($\mu_{a_{x \rightarrow m}}$). In addition, the assumption of a homogeneous and constant $\phi (=0.016)$ could possibly account for the overestimation of $\mu_{a_{x \rightarrow m}}$ values in the Case 3, and the underestimation of $\mu_{a_{x \rightarrow m}}$ values in Cases 1 and 2.

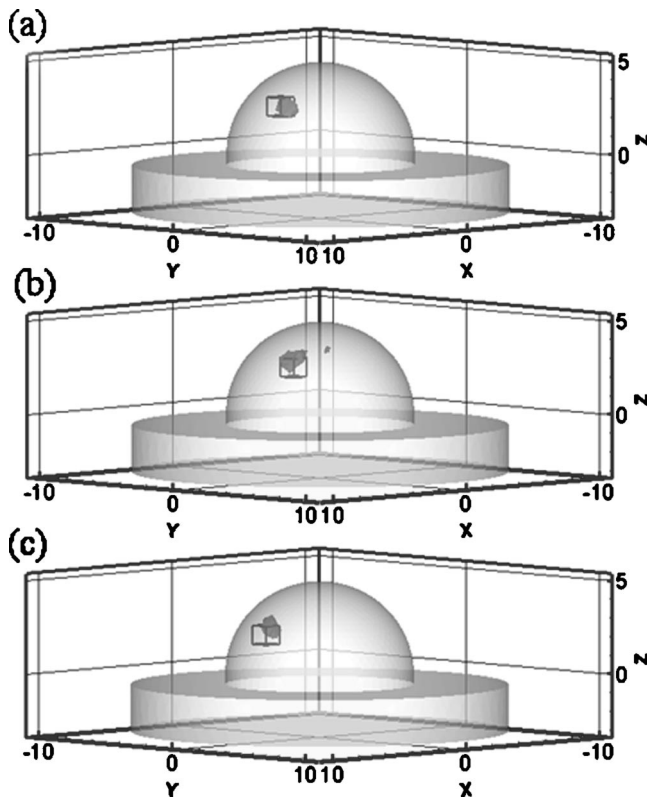


FIG. 3. Three-dimensional iso-surface plots of fluorescence absorption ($\mu_{a_{xf}}$) distributions for (a) Case 1, (b) Case 2, and (c) Case 3. The reconstructed target (solid region inside breast phantom) was differentiated from background phantom at iso-surface cutoff values of 30% of the maximum reconstructed $\mu_{a_{xf}}$ in each case. The true 1 cc volume target is shown by a black wire frame.

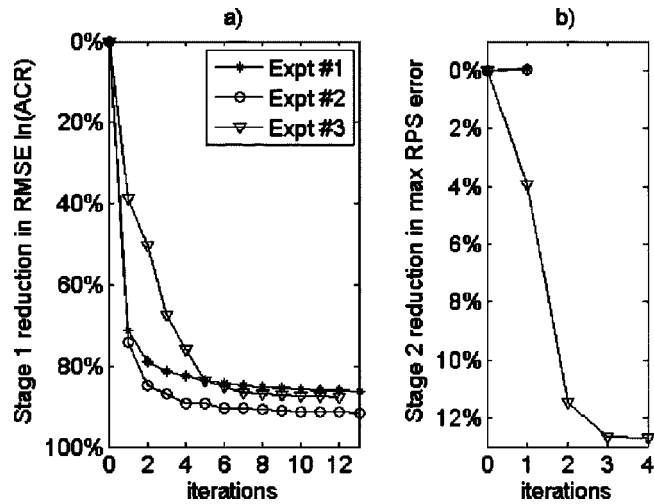


FIG. 4. Normalized convergence plots for (a) Stage-1 and (b) Stage-2 reconstructions, and for all three experimental cases.

C. Three-dimensional fluorescence lifetime tomography

In experimental cases 1 and 2, where there was no T:B fluorescence lifetime contrast, stage-2 reconstructions converged after one iteration, with less than 0.07% change in maximum RPS error [see Fig. 4(b)] and correctly estimated essentially no lifetime contrast (Table IV), demonstrating the specificity of lifetime-based tomography. In Case 3, where there was a 2.1:1 fluorescence lifetime contrast, stage-2 reconstructions converged in four iterations with a 16.5% decrease in maximum RPS error [see Fig. 4(b)] and reconstructed a 2.2:1 T:B lifetime contrast ratio (see Fig. 5 and Table IV). Three-dimensional fluorescence lifetime distributions for Case 3 are shown as a 3D iso-surface plot in Fig. 5(a) and as orthogonal contour slices through the true centroid of the target in Figs. 5(b)–5(d). A few heterogeneities were observed in the phantom background [see Fig. 5(c)], whose maximum reconstructed τ values were less than 25% of the maximum reconstructed τ value in the target location. Hence, these heterogeneities were not classified as artifacts [Fig. 5(a)] in the current studies.

In order to test the sensitivity of our stage-2 lifetime reconstructions to the quantitative errors in the stage-1 fluorescence absorption reconstructions, a separate study was carried out. Stage-2 (lifetime) reconstructions from

TABLE IV. Reconstructed T:B contrast values of fluorescence absorption ($\mu_{a_{x \rightarrow m}}$) and lifetime (τ) for all experimental cases. Max(T):B corresponds to maximum reconstructed value of the optical parameter in the target relative to the background.

Case	$\mu_{a_{x \rightarrow m}}$ (cm^{-1}) max(T):B		τ (ns) max(T):B	
	Estimated	Actual	Estimated	Actual
1	0.09 : 0.001	0.30 : 0.003	0.564 : 0.560	0.560 : 0.560
2	0.38 : 0.001	0.30 : 0.003	0.567 : 0.560	0.560 : 0.560
3	0.78 : 0.001	0.21 : 0.003	1.25 : 0.560	1.18 : 0.560

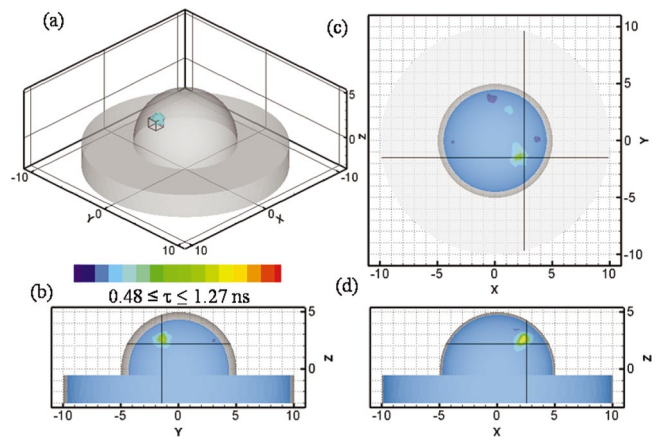


FIG. 5. Four views of the 3D fluorescence lifetime reconstructions for Case 3. (a) 3D iso-surface plot of the lifetime distribution (iso-surface cutoff at 30% of the maximum lifetime value with respect to background lifetime), (b)–(d) orthogonal contour slices through the true centroid location (shown by white crosshairs).

experimental measurements of RPS were carried out using three levels of assumed T:B $\mu_{a_{x \rightarrow m}}$ contrasts of (i) 0.03:0.003, (ii) 0.3:0.003, and (iii) 0.7:0.003 (all in cm^{-1}), for all three experimental cases. Except for the assumed T:B $\mu_{a_{x \rightarrow m}}$ contrast levels in each experimental case, the remaining parameter settings were the same as those described in Sec. II C for stage-2 reconstructions.

The maximum reconstructed T:B fluorescence lifetime contrasts obtained using the assumed (and deliberately incorrect) T:B $\mu_{a_{x \rightarrow m}}$ contrast values at various levels are presented as a bar plot in Fig. 6. It can be seen from the bar plot that the stage-2 lifetime reconstructions detected no lifetime contrast in the target for Cases 1 and 2 (suggesting high specificity) but detected an elevation in lifetime (as expected) in the target for Case 3, regardless of the absolute value of T:B $\mu_{a_{x \rightarrow m}}$ contrast levels assumed. These results further validate that 3D lifetime tomography can detect small (2.1:1) lifetime contrasts, and is relatively insensitive to the quantitative errors in the reconstructed fluorescence absorption ($\mu_{a_{x \rightarrow m}}$).

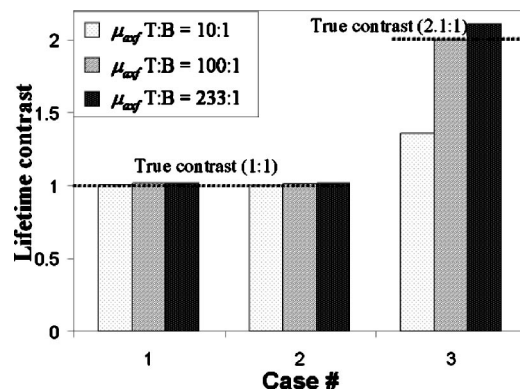


FIG. 6. Bar plot of the Stage 2 reconstructed (maximum value of) T:B lifetime contrast for Cases 1, 2, and 3, imposing three different levels of rescaled contrast in the true fluorescence absorption structure.

It is worth noting that additional experiments were performed (not otherwise reported here), where reconstruction of $\mu_{a_{x \rightarrow m}}$ was performed in stage 1 using both fluorescence amplitude and phase delay measurements. Since the resulting $\mu_{a_{x \rightarrow m}}$ estimates were very similar to those using amplitude alone, and the subsequent estimates of τ are insensitive to quantitative errors in $\mu_{a_{x \rightarrow m}}$, a more computationally efficient version of stage-1 reconstruction that used only fluorescence amplitude, but not phase delay measurements was employed for the current studies.

IV. SUMMARY AND CONCLUSIONS

The feasibility of 3D fluorescence lifetime tomography in breast phantom volumes was demonstrated using a gain-modulated ICCD imaging system and a two-stage Bayesian reconstruction algorithm. Feasibility studies were carried out both in the presence and absence of fluorescence lifetime contrast in breast phantoms. Fluorescing targets (1 cm³) containing ICG and/or DTTCI contrast agents were embedded 1.4–2.0 cm below the hemispherical surface of the tissue phantoms (1087 cm³ volume) with (i) T:B absorption contrast of 100:1 (Cases 1 and 2) or 70:1 (Case 3) and (ii) T:B fluorescence lifetime contrast of 1:1 (Cases 1 and 2) or 2.1:1 (Case 3). A two-stage reconstruction algorithm was employed to sequentially estimate the spatial distribution of fluorescence absorption followed by fluorescence lifetime, in the entire phantom. All the experimental cases reconstructed the targets close to the actual target locations, based on contrast observed in both $\mu_{a_{x \rightarrow m}}$ and τ distributions. The insensitivity of 3D lifetime tomography to the quantitative errors in $\mu_{a_{x \rightarrow m}}$ distributions was also demonstrated.

Herein, we have presented a three-dimensional tomographic analog to 2D *fluorescence lifetime imaging* microscopy that could extend measurement of fluorescence lifetime of NIR fluorophores deep into tissues and other scattering media. Fluorescence lifetime tomography makes possible the detection of changes in fluorescence resonance energy transfer between donor-acceptor pairs tethered on protease-specific peptides or receptor ligands as well as the quenching of closely tethered fluorophores that can act as “beacons” upon enzyme-specific cleavage of fluorophores.^{22–24} Future work involves determining the minimal fluorescence lifetime contrast required for tomographic imaging as well as the relationship of modulation frequency, depth, and size upon target detectability. Based on these initial phantom studies, there is demonstrated, potential benefit to develop and translate lifetime sensitive agents for *in vivo* diagnostic imaging.

ACKNOWLEDGMENTS

This work was funded in part by the National Institutes of Health Grant Nos. R01 EB 002763 (to M.J.E.) and R01 CA67176 (to E.M.S.).

APPENDIX A

Light propagation and fluorescence generation in tissues can be described using the coupled diffusion equation that

represents the light propagation at excitation and emission wavelengths, respectively. At a given modulation frequency of light, f ($\omega = 2\pi f$ radians), the coupled diffusion equation is given by^{35–37}

$$-\nabla [D_x(\vec{r}) \nabla \Phi_x(\vec{r}, \omega)] + \left[(\mu_{axi} + \mu_{a_{x \rightarrow m}})(\vec{r}) + \frac{i\omega}{c_x} \right] \Phi_x(\vec{r}, \omega) = S\delta(\vec{r} - \vec{r}_s), \quad (A1)$$

$$-\nabla [D_m(\vec{r}) \nabla \Phi_m(\vec{r}, \omega)] + \left[(\mu_{ami} + \mu_{amf})(\vec{r}) + \frac{i\omega}{c_m} \right] \Phi_m(\vec{r}, \omega) = \phi \mu_{a_{x \rightarrow m}} \frac{1}{1 - i\omega\tau} \Phi_x(\vec{r}, \omega). \quad (A2)$$

In the above equations, Φ_x and Φ_m are the ac components of the excitation and emission fluence (photons/s cm²) respectively; D is the diffusion coefficient (cm²); μ_{axi} is the absorption coefficient due to the chromophores (cm⁻¹) (i.e., the endogenous chromophores in tissues); $\mu_{a_{x \rightarrow m}}$ is the absorption cross section due to the fluorophores [i.e., exogenous fluorescing agents (cm⁻¹)]; μ_{am} represents the absorption coefficient of the emission light due to the chromophores (cm⁻¹); and ϕ and τ denote the quantum efficiency and lifetime (ns) of the fluorophore, respectively. The terms c_x and c_m represent the velocity of light at excitation and emission wavelengths (cm/s); ω corresponds to the modulation frequency of propagating light ($=2\pi f$ rad); and r and r_s are the positional vectors at a given point and source illumination point, respectively. The excitation fluence Φ_x couples the diffusion Eqs. (A.1) and (A.2). In the frequency-domain, fluence at excitation and emission wavelengths are given by $\Phi_x = I_{ac,x} \exp(i\theta_x)$ and $\Phi_m = I_{ac,m} \exp(i\theta_m)$, respectively. Here I_{ac} is the amplitude and θ is the phase shift at excitation (suffix “x”) and emission (suffix “m”) wavelengths, respectively.

The forward model of the light propagation in 3D is solved using the Galerkin approximation of the finite element method and the partial current boundary conditions.³⁸ Here, all the optical properties of the tissue medium and the fluorescing agent are assumed to be known *a priori*, and the fluence is calculated in terms of amplitude and phase shift. Having validated the coupled diffusion equations for the current experimental data (by comparing the experimental data to the simulated measurements), 3D image reconstructions were carried out using the AEKF algorithm (described in Appendix B).

APPENDIX B

Three-dimensional image reconstructions were carried out using a computationally efficient variant of the approximate extended Kalman filter (AEKF) algorithm, which is shown by a generic pseudo-code in Fig. 7. Initially the unknown parameter (here, transformed fluorescence absorption or lifetime) updates (given by $\Delta \mathbf{y}$) are initialized (line 2). The forward simulator, f (line 4) computes predictions of $\ln(\text{ACR})$ and RPS (given by \mathbf{x}) at various locations (1 to m_s) of de-

AEKF pseudocode

```

1: iterate
2:  $\Delta \mathbf{y} = \mathbf{0}$ 
3: for each excitation source  $s$ 
4:  $\mathbf{x} \leftarrow f(\mathbf{y}, s)$ 
5:  $\mathbf{J} \leftarrow \frac{\partial \mathbf{x}}{\partial \mathbf{y}}$ 
6:  $\mathbf{K} \leftarrow (\mathbf{J} \cdot \mathbf{P})^T \cdot (\mathbf{R}_s + \mathbf{Q}_s + \mathbf{J} \cdot \mathbf{P} \cdot \mathbf{J}^T)^{-1}$ 
7:  $\Delta \mathbf{y} \leftarrow \Delta \mathbf{y} + \mathbf{K} \cdot (\mathbf{z}_s - \mathbf{x})$ 
8:  $P_{ii} \leftarrow P_{ii} - \sum_{j=1}^{m_s} K_{ij} \cdot J_{ji} \cdot P_{ii}, \quad \forall i=1..n$ 
9: end for
10:  $\mathbf{y} \leftarrow \mathbf{y} + \Delta \mathbf{y}$ 
11: until converged

```

FIG. 7. Generic pseudocode for a computationally efficient version of the approximate extended Kalman filter (AEKF) algorithm.

tected measurements of $\ln(\text{ACR})$ and RPS (given by \mathbf{z}_s), in response to a given excitation source illumination (subscript s) and using the current estimates (i.e., initial estimates in the first iteration) of unknown optical parameters (given by \mathbf{y}). Parameter updates $\Delta \mathbf{y}$ were computed (line 7) by weighting discrepancies between measurements (\mathbf{z}_s) and predictions (\mathbf{x}), based on a nearly-optimal gain matrix (\mathbf{K}). The gain matrix (\mathbf{K}) was computed (line 6) from the Jacobian sensitivity matrix (\mathbf{J}) (line 5) using a Bayesian minimum-variance nonlinear least-squares formulation that was damped by the inverse of a recursively updated (line 8) parameter error covariance (\mathbf{P}), and weighted by the inverse of the sum of the experimentally determined measurement error covariance (\mathbf{R}_s) and an estimate of the model error covariance (\mathbf{Q}_s). After all sources have contributed to the parameter update $\Delta \mathbf{y}$ (loop 3-9), the parameter \mathbf{y} is updated (line 11). This implementation of the AEKF is an approximation to the optimal (minimum-variance) estimate in that (i) we ignore spatial cross covariances (i.e., \mathbf{P} , \mathbf{Q} , and \mathbf{R} are diagonal matrices, hence the update of only the diagonal elements of \mathbf{P} in line 8) and (ii) we have decomposed the data by source (loop 3-9) in order to reduce memory requirements. Additional details on the forward simulator and adjoint sensitivity calculations^{19,38} and AEKF^{14,16,28} are provided elsewhere.

^{a)}Current address: Department of Biomedical Engineering, Florida International University EC 2675, 10555 W. Flagler Street, Miami Florida 33174 USA; electronic mail: godavart@fiu.edu

¹M. A. Franceschini, K. T. Moesta, S. Fantini, G. Gaida, E. Gratton, H. Jess, W. W. Mantulin, M. Seeber, P. M. Schlag, and M. Kaschke, "Frequency-domain techniques enhance optical mammography: Initial clinical results," *Proc. Natl. Acad. Sci. U.S.A.* **94**, 6468–6473 (1997).

²S. Fantini, S. A. Walker, M. A. Franceschini, M. Kaschke, P. M. Schlag, and K. T. Moesta, "Assessment of the size, position, and optical properties of breast tumors *in vivo* by noninvasive optical methods," *Appl. Opt.* **37**, 1982–1989 (1998).

³K. T. Moesta, S. Fantini, H. Jess, S. Totkas, M. A. Franceschini, M. Kaschke, and P. M. Schlag, "Contrast features of breast cancer in frequency-domain laser scanning mammography," *J. Biomed. Opt.* **3**,

129–136 (1998).

⁴D. Grosenick, H. Wabnitz, H. H. Rinneberg, K. T. Moesta, and P. M. Schlag, "Development of a time-domain optical mammograph and first *in vivo* applications," *Appl. Opt.* **38**, 2927–2943 (1999).

⁵S. B. Colak, M. B. van der Mark, G. W. 't Hooft, J. H. Hoogenraad, E. S. van der Linden, and F. A. Kuijpers, "Clinical optical tomography and NIR spectroscopy for breast cancer detection," *IEEE J. Sel. Top. Quantum Electron.* **5**, 1143–1158 (1999).

⁶B. W. Pogue, S. P. Poplack, T. O. McBride, W. A. Wells, K. S. Osterman, U. L. Osterberg, and K. D. Paulsen, "Quantitative hemoglobin tomography with diffuse near-infrared spectroscopy: Pilot results in the breast," *Radiology* **218**, 261–266 (2001).

⁷H. Jiang, Y. Xu, N. Ifimia, J. Eggert, K. Klove, L. Baron, and L. Fajardo, "Three-dimensional optical tomographic imaging of breast in a human subject," *IEEE Trans. Med. Imaging* **20**, 1334–1340 (2001).

⁸E. M. Sevick-Muraca, J. P. Houston, and M. Gurfinkel, "Fluorescence-enhanced, near infrared diagnostic imaging with contrast agents," *Curr. Opin. Chem. Biol.* **6**, 642–650 (2002).

⁹K. Licha, "Contrast agents for optical imaging," *Top. Curr. Chem.* **222**, 1–29 (2002).

¹⁰C. Bremer, V. Ntziachristos, and R. Weissleder, "Optical-based molecular imaging: Contrast agents and potential medical applications," *Eur. Radiol.* **13**, 231–243 (2003).

¹¹V. Ntziachristos and R. Weissleder, "Charge-coupled-device based scanner for tomography of fluorescent near-infrared probes in turbid media," *Med. Phys.* **29**, 803–809 (2002).

¹²V. Ntziachristos and R. Weissleder, "Experimental three-dimensional fluorescence reconstruction of diffuse media by use of a normalized Born approximation," *Opt. Lett.* **26**, 893–895 (2001).

¹³D. J. Hawrysz, M. J. Eppstein, J. Lee, and E. M. Sevick-Muraca, "Error consideration in contrast-enhanced three-dimensional optical tomography," *Opt. Lett.* **26**, 704–706 (2001).

¹⁴M. J. Eppstein, D. J. Hawrysz, A. Godavarty, and E. M. Sevick-Muraca, "Three-dimensional near-infrared fluorescence tomography with Bayesian methodologies for image reconstruction from sparse and noisy data sets," *Proc. Natl. Acad. Sci. U.S.A.* **99**, 9619–9624 (2002).

¹⁵J. Lee and E. M. Sevick-Muraca, "3-D Fluorescence enhanced optical tomography using references frequency-domain photon migration measurements at emission and excitation measurements," *J. Opt. Soc. Am. A* **19**, 759–771 (2002).

¹⁶A. Godavarty, M. J. Eppstein, C. Zhang, S. Theru, A. B. Thompson, M. Gurfinkel, and E. M. Sevick-Muraca, "Fluorescence-enhanced optical imaging in large tissue volumes using a gain modulated ICCD camera," *Phys. Med. Biol.* **48**, 1701–1720 (2003).

¹⁷A. Godavarty, C. Zhang, M. J. Eppstein, and E. M. Sevick-Muraca, "Fluorescence-enhanced optical imaging of large phantoms using single and simultaneous dual point illumination geometries," *Med. Phys.* **31**, 183–190 (2004).

¹⁸A. Godavarty, A. B. Thompson, R. Roy, M. J. Eppstein, C. Zhang, and E. M. Sevick-Muraca, "Progress towards diagnostic imaging of breast cancer using fluorescence-enhanced optical tomography," *J. Biomed. Opt.* **9**, 488–496 (2004).

¹⁹M. J. Eppstein, F. Fedele, J. Laible, C. Zhang, A. Godavarty, and E. M. Sevick-Muraca, "A comparison of exact and approximate adjoint sensitivities in fluorescence tomography," *IEEE Trans. Med. Imaging* **22**, 1215–1223 (2003).

²⁰R. H. Mayer, J. S. Reynolds, and E. M. Sevick-Muraca, "Measurement of the fluorescence lifetime in scattering media by frequency-domain photon migration," *Appl. Opt.* **38**, 4930–4938 (1999).

²¹T. L. Troy and E. M. Sevick-Muraca, "Fluorescence lifetime imaging and spectroscopy in random media," in *Applied Fluorescence in Chemistry, Biology, and Medicine*, edited by Rettig, Strehmel, Schrader, and Seifert (Springer, Berlin, 1999), pp. 3–39.

²²R. Weissleder, C. H. Tung, U. Mahmood, and A. Bogdanov, "In vivo imaging of tumors with protease-activated near-infrared fluorescent probes," *Nat. Biotechnol.* **17**, 375–378 (1999).

²³U. Mahmood, C. H. Tung, A. Bogdanov, and R. Weissleder, "Near-infrared optical imaging of protease activity for tumor detection," *Radiology* **213**, 866–870 (1999).

²⁴M. Funovics, R. Weissleder, and C. H. Tung, "Protease sensors for bioimaging," *Anal. Bioanal. Chem.* **377**, 956–963 (2003).

²⁵J. O. McIntyre, B. Fingleton, K. S. Well, D. W. Piston, C. C. Lynch, S. Gautam, and L. M. Matrisian, "Development of a novel fluorogenic pro-

- teolytic beacon for in vivo detection and imaging of tumour-associated matrix metalloproteinase-7 activity," *Biochem. J.* **377**, 617–628 (2004).
- ²⁶M. A. O'Leary, D. A. Boas, X. D. Li, B. Chance, and A. G. Yodh, "Fluorescence lifetime imaging in turbid media," *Opt. Lett.* **21**, 158–160 (1996).
- ²⁷D. Y. Paithankar, A. U. Chen, B. W. Pogue, M. S. Patterson, and E. M. Sevick-Muraca, "Imaging of fluorescent yield and lifetime from multiply scattered light reemitted from random media," *Appl. Opt.* **36**, 2260–2272 (1997).
- ²⁸M. J. Eppstein, D. E. Dougherty, T. L. Troy, and E. M. Sevick-Muraca, "Biomedical optical tomography using dynamic parameterization and Bayesian conditioning on photon migration measurements," *Appl. Opt.* **38**, 2138–2150 (1999).
- ²⁹R. Roy and E. M. Sevick-Muraca, "A numerical study of gradient-based nonlinear optimization methods for contrast-enhanced optical tomography," *Opt. Express* **9**, 49–65 (2001).
- ³⁰A. B. Milstein, S. Oh, K. J. Webb, C. A. Bouman, Q. Zhang, D. A. Boas, and R. P. Millane, "Fluorescence optical diffusion tomography," *Appl. Opt.* **42**, 3081–3094 (2003).
- ³¹V. Ntziachristos, C. Bremer, C. H. Tung, and R. Weissleder, "Imaging cathepsin B up-regulation in HT-1080 tumor models using fluorescence-mediated molecular tomography (FMT)," *Acad. Radiol.* **9**, S323–S325 (2002).
- ³²E. Shives, Y. Xu, and H. Jiang, "Fluorescence lifetime tomography of turbid media based on an oxygen-sensitive dye," *Opt. Express* **10**, 1557–1562 (2002).
- ³³Z. Sun, Y. Huang, and E. M. Sevick-Muraca, "Precise analysis of frequency-domain migration measurement for characterization of concentrated colloidal suspensions," *Rev. Sci. Instrum.* **73**, 383–393 (2002).
- ³⁴R. Rajagopalan, P. Uetrecht, J. E. Bugaj, S. A. Achilefu, and R. B. Dorshow, "Stabilization of the optical tracer agent indocyanine green using noncovalent interactions," *Photochem. Photobiol.* **71**, 347–350 (2000).
- ³⁵E. M. Sevick-Muraca and C. L. Burch, "Origin of phosphorescence signals reemitted from tissues," *Opt. Lett.* **19**, 1928–1930 (1994).
- ³⁶M. S. Patterson and B. W. Pogue, "Mathematical model for time-resolved and frequency-domain fluorescence spectroscopy in biological tissues," *Appl. Opt.* **33**, 1963–1974 (1994).
- ³⁷C. L. Hutchinson, J. R. Lakowicz, and E. M. Sevick-Muraca, "Fluorescence life-time based sensing in tissues: A computational study," *Biophys. J.* **68**, 1574–1582 (1995).
- ³⁸F. Fedele, J. P. Laible, and M. J. Eppstein, "Coupled complex adjoint sensitivities for frequency-domain fluorescence tomography: Theory and vectorized implementation," *J. Comput. Phys.* **187**, 597–619 (2003).
- ³⁹J. R. Lakowicz, *Principles of Fluorescence Spectroscopy*, 2nd ed. (Plenum Publishers New York, 1999).